Chemical Geology 647 (2024) 121942

Contents lists available at ScienceDirect

Chemical Geology

journal homepage: www.elsevier.com/locate/chemgeo

# Isotopic and geochemical modeling approach to evaluate abiotic nitrite reduction by ferrous iron

Alex Abu [a,b,*], Raúl Carrey [b,c], Dídac Navarro-Ciurana [a,b], Rosanna Margalef-Marti [a,b], Albert Soler [a,b], Neus Otero [a,b,d], Cristina Domènech [a,b]

[a] Grup MAiMA, Mineralogia Aplicada, Geoquímica i Hidrogeologia – MAGH, Departament de Mineralogia, Petrologia i Geologia Aplicada, Facultat de Ciències de la Terra, Universitat de Barcelona (UB), 08028 Barcelona, Spain
[b] Institut de Recerca de l'Aigua (IdRA), Universitat de Barcelona (UB), 08001 Barcelona, Spain
[c] Centres Científics i Tecnològics, Universitat de Barcelona (UB), C/Lluís Solé i Sabarís 1-3, 08028 Barcelona, Spain
[d] Serra Húnter Fellowship. Generalitat de Catalunya, Spain

ARTICLE INFO

Editor: Michael E. Boettcher

*Keywords:*
Chemodenitrification
Isotope fractionation
$N_2O$ site preference
Numerical modeling

ABSTRACT

Nitrite reduction has often been treated as a biotic process in water treatment systems, but it also occurs abiotically, and it is difficult to distinguish both reactions as they can co-occur at field-scale. The potential reduction of $NO_2^-$ was tested in 3 anaerobic experimental scenarios using a $NO_2^-$ bearing solution amended with: i) siderite ($FeCO_3$) (*Sid* experiment); ii) Fe(II) solution from $FeCl_2.4H_2O$(s) (*DFe* experiment); and iii) siderite mixed with Fe(II) solution (*Sid+DFe* experiment). Non-sterilized batch experiments were carried out in anaerobic conditions with an initial ratio of nitrogen to dissolved iron of 5 in DFe and Sid+DFe (Sid had no initially dissolved Fe(II)) and 1000 mg $L^{-1}$ of siderite in Sid and Sid+DFe experiments. At the end of the experiments, the $NO_2^-$ removed was 3% for Sid, 54% for DFe and 84% for Sid+DFe. The $NO_2^-$ concentration decrease over time was characterized by an enrichment in the $\delta^{15}N_{NO2}$ of the unreacted $NO_2^-$, increasing from −26.9 ‰ to −26.4 ‰ (Sid), −18.0 ‰ (DFe) and −15.9 ‰ (Sid+DFe). The calculated $\varepsilon^{15}N_{NO2}$ for Sid was −11.8 ‰, whereas for DFe was −12.0 ‰ and Sid+DFe was −13.0 ‰, suggesting a common $NO_2^-$ degradation mechanism in all experiments. The Rayleigh distillation equation showed that the generated $N_2O$ was the final product of the abiotic nitrite reduction reaction, and the calculated $N_2O$ site preference (SP) was 22.5 ± 0.7 ‰ for DFe and 23.5 ± 0.5 ‰ for Sid+DFe. The continuous $N_2O$ measurement showed that only 25.3 ± 5.1% in DFe and 31.0 ± 6.3% in Sid+DFe of the generated $N_2O$ in water was recovered in the headspace vials, suggesting that a large portion of the produced $N_2O$(aq) in solution did not diffuse from water. The coupled $NO_2^-$ reduction and Fe(II) oxidation followed a second-order kinetic reaction with a rate equal to $(9.39 \pm 0.36)\cdot10^{-4}\cdot[NO_2^-]\cdot[Fe(II)]$ (mol $L^{-1}$ $s^{-1}$) in all experiments. The experimental conditions supported by the Rayleigh distillation equation using the experimentally calculated $\varepsilon^{15}N$ values, coupled with $NO_2^-$ isotopic data and $N_2O$ SP values, showed that biological denitrification had a negligible influence on nitrite reduction and that chemodenitrification was the main $NO_2^-$ attenuation pathway. A geochemical model coupling the kinetic chemodenitrification, isotope fractionation, aqueous speciation in equilibrium and precipitation and dissolution of calcite has been implemented and reproduced the experimental results. The geochemical model developed in our study can be applied to similar experimental studies and to field-scale studies to predict the efficiency of abiotic nitrite reduction treatments using Fe(II).

## 1. Introduction

Groundwater nitrate ($NO_3^-$) pollution, which is attributed principally to agricultural activities, is one of the modern global societal challenges as it causes major environmental and public health problems in many parts of the world (Arauzo, 2017). $NO_3^-$ impairs water quality, and ingesting water containing high $NO_3^-$ or $NO_2^-$ concentrations endangers human life with health hazards, including methemoglobinemia and

* Corresponding author at: Facultat de Ciències de la Terra, Departament de Mineralogia, Petrologia i Geologia Aplicada, Universitat de Barcelona, Martí i Franquès, s/n, 08028 Barcelona, Spain.
*E-mail address:* alexabu@ub.edu (A. Abu).

https://doi.org/10.1016/j.chemgeo.2024.121942
Received 5 July 2023; Received in revised form 15 January 2024; Accepted 16 January 2024
Available online 17 January 2024

gastric and stomach cancer (Fan and Steinberg, 1996; WHO, 2017). Groundwater $NO_3^-$ concentration in many European areas exceeds the safe drinking water threshold of 50 mg $L^{-1}$ of $NO_3^-$ and requires the application of induced remediation methods (EU parliament, 2020). Groundwater $NO_3^-$ attenuation occurs mainly through natural or induced biological denitrification, where $NO_3^-$ is reduced to gaseous products, generating nitrite ($NO_2^-$) as an intermediate product (Fig. 1). Other biotic processes, such as dissimilatory nitrate reduction to ammonium (DNRA), anaerobic ammonium oxidation (anammox), nitrifier denitrification and nitrification, also contribute to groundwater nitrite transformation processes (Fig. 1).

Nitrite reduction was often reported to be microbially catalyzed, but recent findings have proven that $NO_2^-$ is chemically reactive and can also be abiotically reduced to $N_2O$ by Fe(II) oxidation in anaerobic conditions (Chen et al., 2020a; Liu et al., 2019; Wankel et al., 2017). Iron is a common redox-active metal in the environment (Kappler and Straub, 2005), which occurs as dissolved, sorbed or structural Fe(II). Fe and N redox cycles are frequently interrelated, affecting N compound transformations in groundwater (Emerson et al., 2010). The oxidation of Fe (II) to Fe(III), mediated by nitrate-dependant bacteria, uses $NO_3^-$ as an electron acceptor (Bryce et al., 2018), producing nitrite as an intermediate product. Sørensen and Thorling (1991) and Picardal (2012) reported simultaneous biotic and abiotic $NO_2^-$ reduction during biological denitrification in batch cultures. Therefore, in Fe-rich environments, the biotic-abiotic processes might co-occur, and the former process may further reduce the $N_2O$ produced by the latter process to $N_2$. Quantifying the biotic and abiotic components of $NO_2^-$ reduction is significant to understand the geochemical coupling of N and Fe redox cycles and to evaluate the potential efficiency of nitrate remediation strategies using Fe(II) (Kopf et al., 2013; Liu et al., 2019).

Stable isotopes of N ($\delta^{15}N$) and O ($\delta^{18}O$) have proven to be an effective tool for characterizing and quantifying environmental transformations of N compounds (Kendall et al., 2007; Margalef-Marti et al., 2020). Dual isotope systematics of $NO_2^-$ transformation has been characterized during biological denitrification (Grau-Martínez et al., 2019; Martin and Casciotti, 2016), nitrification (Granger and Wankel, 2016; Sebilo et al., 2006), nitrifier denitrification (Ostrom and Ostrom, 2012; Wrage et al., 2001), anammox (Casciotti et al., 2010) and $NO_2^-$ reoxidation to $NO_3^-$ (Buchwald and Casciotti, 2010). The kinetic isotope effect of N and O linked with chemodenitrification, which represents an essential control on $NO_2^-$ isotopic composition in Fe-rich environments, has not been the object of research until recently and less information is available compared to biological processes (Buchwald et al., 2016; Jones et al., 2015; Martin and Casciotti, 2016; Sebilo et al., 2019). During nitrite reduction (biotic and abiotic), the light N and O isotopes preferentially react faster, leading to the accumulation of the heavy isotopes of the unreacted nitrite ($^{15}N_{NO2}$ and $^{18}O_{NO2}$), which differentiates chemodenitrification and denitrification from processes that do not alter changes in the nitrite isotopic composition, such as mixing or dilution (Kopf et al., 2013). Consequently, the heavy isotopes of the generated $N_2O$ ($^{15}N_{N2O}$ and $^{18}O_{N2O}$) progressively increase, approaching the initial $NO_2^-$ isotopic composition in the case of the chemodenitrification, as it is the final product of the reaction. However, it is not still clear if it is possible to distinguish the biotic from the abiotic reactions as both processes show similar patterns of isotopic fractionation. The site preference (SP) of the generated $N_2O$ and geochemical numerical modeling, including isotopic data, are promising tools that could be helpful to distinguish biotic and abiotic processes after coupling with all other data. Coupling the isotopic characterization of $NO_2^-$ and $N_2O$ could, therefore, be useful in identifying the nitrous oxide production pathway.

The two N atoms of $N_2O$ differ in the nature of their covalent bonds and tend to acquire distinct isotopic compositions. The difference in $\delta^{15}N$ between the central N atom (Nα) and outer N atom (Nβ) of $N_2O$ (Nβ-Nα-O) provides site-specific isotopic information. SP does not depend on the isotopic composition of the substrate ($NO_2^-$ in the case of chemodenitrification) and does not exhibit fractionation during its production, making SP a powerful indicator of the $N_2O$ production pathway (Heil et al., 2014; Jones et al., 2015). $N_2O$ SP values have successfully been used as indicators of nitrifier denitrification (−10 to 0 ‰), hydroxylamine oxidation and fungal denitrification (33 to 37 ‰), heterotrophic denitrification (−5 to 5 ‰) as sources of $N_2O$ (Li et al., 2022; Ostrom and Ostrom, 2012).

Numerical simulations provide an essential tool for research in contaminant degradation processes, which allows the quantitative evaluation of complex processes. They also serve to predict the extent and consequences of geochemical reactions, interpret experimental data and test scenarios beyond laboratory experiment ranges, and for field-scale application (Zhu, 2012). While Monod kinetic equations are often used in modeling biotic $NO_2^-$ reduction (Betlach and Tiedje, 1981), the kinetic model approach has been developed to characterize abiotic nitrite reduction and include pseudo-first-order, second-order nitrite degradation rate equations and others (Benaiges-Fernandez et al., 2020;

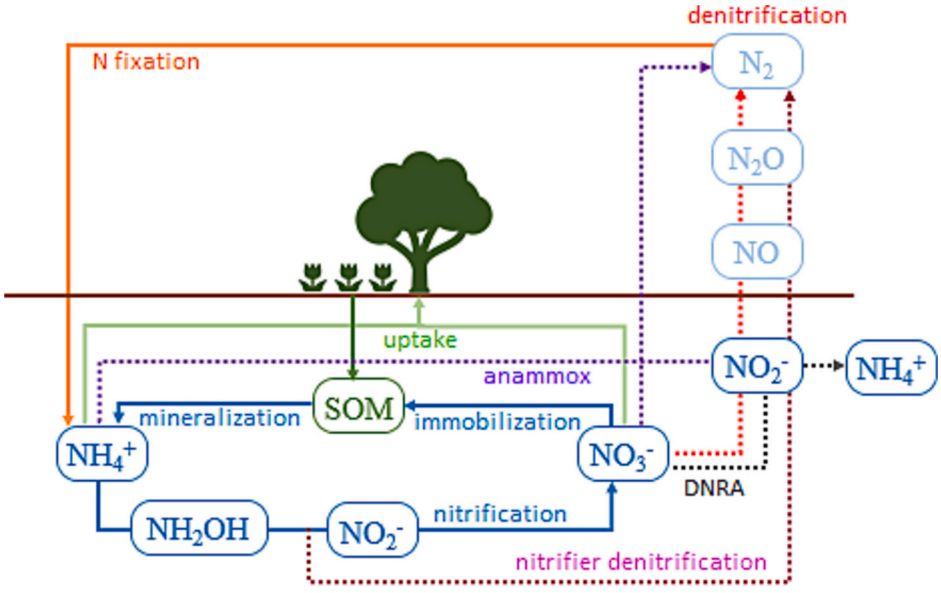


**Fig. 1.** Schematic model of N transformation pathways in aerobic (continuous lines) and anaerobic (dotted lines) conditions. SOM is soil organic matter (Modified after Margalef-Marti et al., 2021).

Liu et al., 2019). Despite several studies applied isotopic tools to identify and quantify the degradation pathways of $NO_2^-$, only a few studies focused on quantifying the isotope fractionation of $NO_2^-$ during abiotic $NO_2^-$ reduction by Fe(II) (Chen et al., 2021; Kopf et al., 2013). Therefore, improving the abiotic $NO_2^-$ reduction numerical model is essential to understand the geochemical processes controlling N transformations.

Siderite, the most common iron carbonate mineral, can be used as a larger reservoir of Fe(II) with high dissolution rate to catalyze natural and induced denitrification in polluted water (Dunlop and Özdemir, 2015; Nowak et al., 2023). Siderite was consequently chosen in the present work to investigate its effect on abiotic batch experiments with particular emphasis on nitrite reduction and nitrous oxide production dynamics. Dissolved synthetic Fe(II) was also added in some of the experiments to assess its potential to increase the reactivity. Three scenarios (only siderite (Sid), only dissolved iron II (DFe) and dissolved iron + siderite (Sid+DFe)) were tested. Isotopic tools were employed to characterize nitrite attenuation and compare the calculated fractionation values to the range of values reported in the literature for different nitrite reduction processes. The fractionation values were then applied to the numerical modeling. Based on our knowledge, combining laboratory experiments with the dual $NO_2^-$ and $N_2O$ isotope modeling has never been applied so far in chemodenitrification. In this context, we also aim to develop a conceptual and numerical geochemical model that can reproduce our experimental results in order to upscale it to future field-scale studies.

## 2. Materials and methods

### 2.1. Experimental setup

Three parallel sets of anaerobic batch experiments, named Sid, DFe, and Sid+DFe, were performed under non-sterile conditions using 25 mL headspace (HS) vials. Based on preliminary batch experiments tests, 13 vials were chosen for the DFe and Sid+DFe experiments, while 4 vials were chosen for Sid experiments (negligible or extremely low reactivity was observed in the absence of DFe). Each vial for the Sid experiment was filled with 10 mg of micro-sized siderite and mixed with 10 mL of synthetic groundwater (SW, Table 1) prepared to simulate field conditions. Vials for DFe experiments were filled with 10 mL of SW and amended with 10 mg of $FeCl_2.4H_2O$(s), and vials for Sid+DFe experiments were filled with 10 mg of siderite, mixed with 10 mL of the SW and amended with 10 mg of $FeCl_2.4H_2O$(s). An initial ratio between N and dissolved Fe(II) of 5 was kept in DFe and Sid+DFe experiments, while no dissolved Fe was added in the Sid experiments. Each vial was immediately crimped with a butyl rubber stopper and purged with Argon gas during the first two minutes to create anaerobic conditions. All the batch experiments were carried out at ambient temperatures (18 °C to 25 °C) and kept in darkness under continuous shaking to avoid photodegradation processes. They lasted 8 days based on the preliminary batch experiments, and duplicate vials for each treatment set were sacrificed in turns at different times.

**Table 1**
Composition of the synthetic water (SW) and the mass concentration of reagents used to prepare it. * only in DFe and Sid+DFe experiments.

| Chemical | mol $L^{-1}$ | Reagent | mol $L^{-1}$ |
|---|---|---|---|
| pH | 7.60 | $NaHCO_3^-$ (Sigma-aldrich 99.5%) | $3.60{\cdot}10^{-3}$ |
| pe | −3.00 | $KH_2PO_4$ (Alfa aesar 98–100.5%) | $0.04{\cdot}10^{-3}$ |
| Ca | $8.77{\cdot}10^{-4}$ | $MgCl_2.6H_2O$ (Sigma-aldrich 99–102%) | $1.24{\cdot}10^{-3}$ |
| Mg | $1.24{\cdot}10^{-3}$ | KCl (Sigma-aldrich 99%) | $1.50{\cdot}10^{-3}$ |
| K | $2.55{\cdot}10^{-3}$ | $CaCl_2.2H_2O$ (Pancreac 74–80%) | $8.77{\cdot}10^{-3}$ |
| Na | $6.44{\cdot}10^{-3}$ | $Na_2SO_4$ (Alfa aesar 99%) | $1.42{\cdot}10^{-3}$ |
| S | $1.42{\cdot}10^{-3}$ | $KNO_2$ (Alfa aesar >96%) | $1.01{\cdot}10^{-3}$ |
| C | $3.60{\cdot}10^{-3}$ | $FeCl_2{\cdot}4H_2O$ (Pancreac 98%) | $5.03{\cdot}10^{-3}$* |
| P | $3.67{\cdot}10^{-5}$ | | |
| $Cl^-$ | $5.75{\cdot}10^{-3}$ | | |
| $NO_2^-$ | $1.2{\cdot}10^{-3}$ | | |

### 2.2. Analytical methods

Samples obtained from conducted experiments were prepared for chemical and isotopic analyses at the laboratory of the MAiMA-UB research group and analyzed at the Centres Científics i Tecnològics of the Universitat de Barcelona (CCiT-UB). The headspace of each vial was first extracted using a gas syringe and stocked in exetainer flasks for subsequent $N_2O$ concentration and isotopic analyses. After obtaining the gaseous samples, the headspace vials were decapsulated, and the liquid fraction was obtained and filtered using the 0.22 μm Millipore® PTFE hydrophilic syringe filters. One aliquot of the filtered liquid fraction was immediately used to convert $NO_2^-$ to $N_2O$ using the azide reduction method for $NO_2^-$ concentration and isotope analysis (McIlvin and Altabet, 2005; Ryabenko et al., 2009). Nitrite concentration standards were then analyzed to calculate the samples' nitrite and nitrous oxide concentrations from the samples' peak amplitudes determined by isotope ratio mass spectroscopy (IRMS), as illustrated in Fig. S1 and summarized in Table S1. We employed this method to avoid issues associated with the oxidation of Fe(II) to Fe(III) and the subsequent precipitation of Fe (III) oxy(hydr)oxides in water and to prevent any possible reduction reactions of nitrite that might persist after the vials were sacrificed. Two vials were sacrificed at each time point, and each vial sample was analyzed by duplicate. The results at each time correspond to the average of these four measurements.

The isotopic compositions of N ($\delta^{15}N$) and O ($\delta^{18}O$) of dissolved $NO_2^-$ were analyzed following the sodium azide reduction method, which converts $NO_2^-$ to $N_2O$ (McIlvin and Altabet, 2005; Ryabenko et al., 2009), immediately after sample collection to avoid further reduction of $NO_2^-$ or other chemical reactions. The $\delta^{15}N$ and $\delta^{18}O$ composition of the generated $N_2O$ with the sodium azide ($\delta^{15}N_{NO2}$, $\delta^{18}O_{NO2}$) and of the $N_2O$ collected from the HS of the batch experiments were analyzed using a Pre-Con (Thermo Scientific) coupled to an IRMS (Finnigan MAT 253, Thermo Scientific). The bulk and positional isotope of $N_2O$ ($\delta^{15}N^{bulk}_{N2O}$, $\delta^{15}N^{\alpha}_{N2O}$, $\delta^{18}O_{N2O}$, $\delta^{15}N^{\beta}_{N2O}$) were measured using the arrays of mass/charge ratios of 46, 45 and 44 for the $N_2O^+$ molecular ion and 31 and 30 for the $NO^+$ fragment of the $N_2O$ molecule. $\delta^{15}N^{bulk}_{N2O}$ is the bulk $\delta^{15}N$ of $N_2O$, $\delta^{15}N^{\alpha}_{N2O}$ is the isotopic composition of the central N of $N_2O$, and $\delta^{15}N^{\beta}_{N2O}$ is the isotopic composition of the outer N ($N^{\beta}$-$N^{\alpha}$-O). Therefore, the $\delta^{15}N$ of $N_2O^+$ provides the $\delta^{15}N^{bulk}_{N2O}$, the $\delta^{15}N$ of $NO^+$ provides the $\delta^{15}N^{\alpha}_{N2O}$, and the $\delta^{15}N^{\beta}_{N2O}$ is derived from Eq. (1). The site preference (SP) of $N_2O$(g) can be then calculated from $\delta^{15}N^{\beta}_{N2O}$ and $\delta^{15}N^{\alpha}_{N2O}$ according to Eq. (2). Isotopic notation is expressed in terms of $\delta$ (‰) relative to the international standard: atmospheric $N_2$ (AIR) for $\delta^{15}N$ and Vienna Standard Mean Oceanic Water (V-SMOW) for $\delta^{18}O$. Hence, $\delta = \left(R_{sample} - R_{standard}\right)/R_{standard}$, where R is the isotope ratio ($\delta^{15}N/\delta^{14}N$ and $\delta^{18}O/\delta^{16}O$). $NO_2^-$ isotopic composition was calibrated using the UB internal working standard CCiT-IWS ($\delta^{15}N$ = +28.5 ‰, 1σ = ±0.1 for $\delta^{15}N_{NO2}$), which is analyzed at every set of 5 to 6 samples by duplicate. $N_2O$ was calibrated using the international standard USGS-51 ($\delta^{15}N$ = +1.3 ‰, $\delta^{18}O$ = +41.2 ‰, 1σ = ±0.5 for $\delta^{18}O_{N2O}$ and ±0.1 for $\delta^{15}N_{N2O}$).

$$\delta^{15}N^{bulk}{}_{N2O(g)}(‰) = \left(\delta^{15}N^{\alpha}{}_{N2O(g)} + \delta^{15}N^{\beta}{}_{N2O(g)}\right)/2 \quad (1)$$

$$SP\ (‰) = \left(\delta^{15}N^{\alpha}{}_{N2O(g)} - \delta^{15}N^{\beta}{}_{N2O(g)}\right) \quad (2)$$

The kinetic isotope fractionation (ε) associated with nitrite reduction was quantified by the Rayleigh distillation equation (Eq. (3)), where $C_{initial}$ and $C_{residual}$ are the initial and residual nitrite concentration (mol $L^{-1}$), respectively, and $R_{initial}$ and $R_{residual}$ are the isotope ratios of the initial and residual nitrite.

$$Ln\left(\frac{R_{residual}}{R_{initial}}\right) = \varepsilon \cdot Ln\left(\frac{C_{residual}}{C_{initial}}\right) \quad (3)$$

### 2.3. Numerical method

Geochemical calculations and modeling have been carried out with the GibbsStudio software (Nardi and de Vries, 2017) based on PHREEQC version 3 code (Parkhurst and Appelo, 2013) and the iso.dat and wateq4f.dat databases supplied with the PHREEQC code. GibbsStudio helped to manage water chemistry sample data and run PHREEQC models in a unified productive graphical environment.

## 3. Results and discussion

### 3.1. $NO_2^-$ attenuation dynamics

Low nitrite reduction was identified in the batch experiments containing only siderite, as only 3% of $NO_2^-$ was removed (Fig. 2A), which is similar to experimental results conducted with other similar Fe(II) mineral compounds (siderite, magnetite, olivine) by Margalef-Marti et al. (2020) and Rakshit et al. (2008). However, in the conducted experiments involving DFe and Sid+DFe treatments, higher rates of $NO_2^-$ reduction were observed. 54% and 84% of $NO_2^-$ were removed in DFe and Sid+DFe, respectively, as $NO_2^-$ levels decreased from an initial concentration of 1.10 mM to 0.51 mmol $L^{-1}$ in DFe, and to 0.17 mmol $L^{-1}$ in Sid+DFe (Fig. 2A).

Nitrite reduction in the batch experiments led to generation of gaseous nitrous oxide in the vial headspaces. $N_2O$(g) rarely accumulated in the Sid experiment but increased to 0.187 mmol $N_2O$(g)/L $H_2O$ and 0.194 mmol $N_2O$(g)/L $H_2O$ in DFe and Sid+DFe, respectively, on day 7 (Fig. 2B).

In our experiments, we did not use sediments or add microorganisms, and the absence of these biological components substantially restricts the potential for biological denitrification. Additionally, the relatively short duration of our experiments limits biological processes. Microbial denitrification, in the absence of sediments or added microorganisms, necessitates an extended period for microbial populations to establish and promote substantial nitrite reduction. A study by Visser et al. (2020) and Margalef-Marti et al. (2020) demonstrated that biological denitrification, without sediments or microbial inoculation, progresses slowly, with less than a 3% nitrite reduction rate observed over approximately 200 days. Fe(II) is recognized for inducing slower rates of biological denitrification compared to organic carbon sources (Rahman et al., 2019), which diminishes the likelihood of significant biological denitrification occurring within our experimental conditions. Consequently, we have considered that our experimental conditions are abiotic. Considering abiotic nitrite reduction, N-$NO_2^-$ attenuation and N-$N_2O$ production are expected in a 1:1 stoichiometry according to reaction (R1).

$$2NO_2^- + 6H^+ + 4e^- \rightarrow N_2O\,(g) + 3H_2O \quad (R1)$$

However, the nitrous oxide recovered in the vial headspaces in our experiments did not match the expected except for the first half of the experiments in Sid, which partially accounted for the $NO_2^-$ removed from the vials (Fig. 3A-C).

The non-stoichiometry may be attributed to the formation of the intermediary compound NO, which may bind to mineral surfaces and prevent further reduction (Collman et al., 2008; Dhakal et al., 2013) or the further reduction of $N_2O$ to $N_2$. The absence of biological components in our experiments restricts the potential $N_2O$ to $N_2$ reduction. Few authors have measured other gases than $N_2O$, and when measured, only minimal to no NO or $N_2$ nitrogen mass recoveries from these other gases were identified (Buchwald et al., 2016; Dhakal et al., 2021; Kampschreur et al., 2011; Rakshit et al., 2016; Wankel et al., 2017). Another process that might have contributed to the non-stoichiometry of the expected and measured $N_2O$ is the leakage of $N_2O$ through the butyl rubber stoppers or the low diffusion of aqueous $N_2O$ into the HS. The reduced recoveries in our current study may be linked to the low diffusion of $N_2O$ into the vial's headspace, potentially influenced by metal chlorides in the prepared water. Previous studies have shown that halides, including metal chlorides, can impact $N_2O$ recoveries (Ryabenko et al., 2009). Several authors have observed a non-stoichiometry between N-$NO_2^-$ removed and generated N-$N_2O$(g) during $NO_2^-$ reduction, as a wide range of gaseous $N_2O$ recoveries has been reported. In fact, <50% of N-$NO_2^-$ removed during nitrite reduction is usually recovered as N-$N_2O$(g) in abiotic conditions (Chen et al., 2020a; Dhakal et al., 2021; Jones et al., 2015; Rakshit et al., 2016). In the present experiments, the $N_2O$ recovery decreased from 36% to 19% in Sid+DFe, and significant fluctuations have been observed in DFe, with a maximum recovery rate (46%) at 36 h and a recovery rate of 25% on day 7 (Fig. 3D). The formation of iron oxide minerals may sorb $NO_2^-$ intermediate reduction product (NO) or Fe (II), influencing $N_2O$(g) production and transformation (Chen et al., 2020a; Jones et al., 2014, 2015), which may explain changes in the recovery rate over time. N-$N_2O$ in the liquid phase (undiffused N-$N_2O$) in the experiments of Sid+DFe accounted for 50–96% of the transformed N in the water and 68 to 98% in DFe experiments (Table S2). N-$N_2O$ in the gas and liquid phases and the residual N-$NO_2^-$ always equal the initial $NO_2^-$ concentration in all the experiments. This indicates that $N_2O$ leakages through the butyl rubber stoppers, the formation of intermediary NO, and the reduction of $N_2O$ to $N_2$(g) did not occur in our experiments. Consequently, we can conclude that the main reason for not observing 100% $N_2O$ recovery in the headspace vials is the solubility of $N_2O$ in water, which retained a larger portion of the $N_2O$. The percentage of total N-$N_2O$ compared to the total N varied from 2.3 to 60.0% in Sid+DFe and 0.2 to 61.3% in DFe experiments (Table S2).

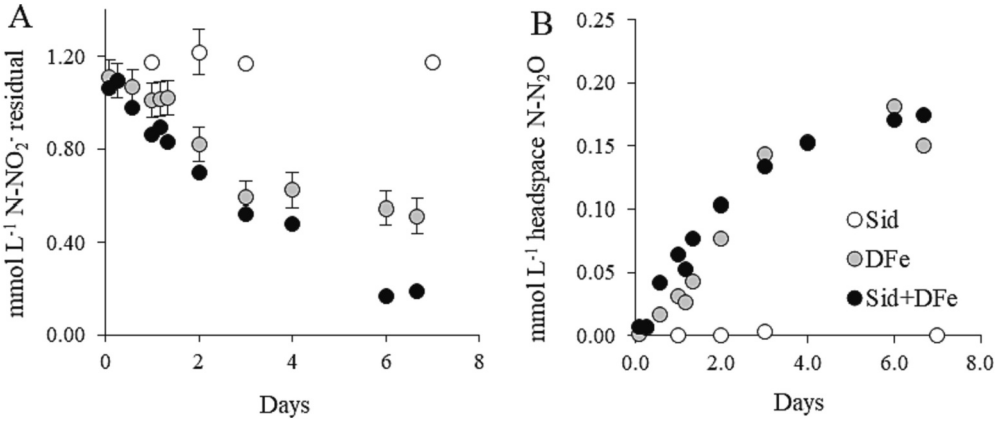


**Fig. 2.** A) Evolution of residual $NO_2^-$ in solution. B) Evolution of $N_2O$(g) recovered in vial headspaces. The error bars represent the standard error (SE) of duplicate samples, and non-visible error bars are small and embedded within the data points.

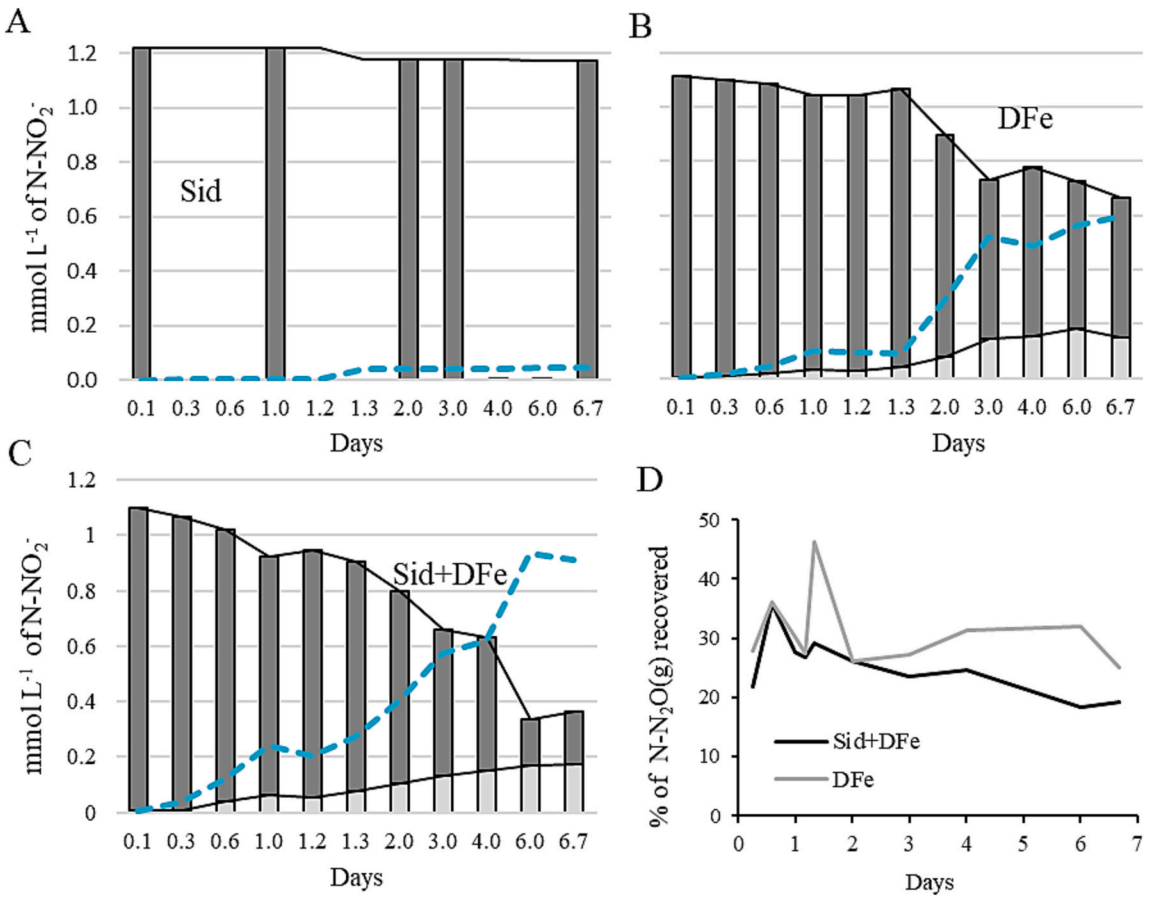


**Fig. 3.** Bar graphs showing the distribution of the residual $NO_2^-$ (dark grey bars), the recovered N-$N_2O$(g) (light grey bars), and the N-$N_2O$ expected from the degradation of $NO_2^-$ (transformed N-$NO_2^-$) (dashed lines) in the experiments of Sid (A), DFe (B) and Sid+DFe (C). D) The percentage distribution of recovered $N_2O$ over time.

$NO_3^-$ was monitored with paper test stripes and was consistently below the detection limit. However, $NH_4^+$ was not measured. The initial prepared water did not contain $NH_4^+$, and we did not consider the possibility of DNRA since $NO_3^-$ was not present, discarding $NH_4^+$ formation in our experiments through DNRA or through nitrite abiotic reduction. Furthermore, in previous nitrite reduction experiments, $NH_4^+$ has often not been detected (Margalef-Marti et al., 2020; Rakshit et al., 2016).

Nitrite reduction in this study was linked with a $\delta^{15}N_{NO2}$ enrichment over time. A significant $\delta^{15}N_{NO2}$ increase was observed in DFe and Sid+DFe experiments for the first two and a half days, corresponding to the period marked by high nitrite degradation, and remained in a steady state afterwards (Fig. 4A). $\delta^{15}N_{NO2}$ values increased from −26.9 to −26.4 ‰ (Sid), −18.0 ‰ (DFe) and −15.9 ‰ (Sid+DFe) (Table S3). Due to $\delta^{18}O_{NO2}$ equilibration with $\delta^{18}O_{H2O}$ during $NO_2^-$ reduction, the obtained $\delta^{18}O_{NO2}$ values in this study were not correlated with the residual $NO_2^-$ concentration (Supplementary Information). For this reason, no further discussion is provided on the $\delta^{18}O_{NO2}$ or $\delta^{18}O_{N2O}$ results. The $\delta^{15}N^{bulk}$ values of the generated $N_2O$(g) increased over time, with the most significant increment identified during the first two and a half days: $\delta^{15}N^{bulk}$ composition increased from −52.6 to −36.5 ‰ in DFe and from −57.1 to −38.6 ‰ in Sid+DFe (Fig. 4B).

The transformation of nitrogen oxides is often characterized by kinetic isotope fractionation (Mariotti et al., 1981), which follows the Rayleigh distillation Eq. (2) in a closed system. The calculated $\varepsilon^{15}N_{NO2}$ values were −11.8 ± 11.0 ‰ (Sid), −12.0 ± 1.4 ‰ (DFe) and −13.0 ± 1.1 ‰ (Sid+DFe) (Fig. 4C). The preliminary batch experiments had shown that nitrite reduction in the Sid experiment was very slow, and duplicate samples were analyzed at only 4 time points, resulting in a large error with the $\varepsilon$ value. Even though its coefficient of determination ($R^2$) is very low, the $\varepsilon$ value is considered to be correct as it is similar to the other two. The similar $\varepsilon$ values obtained suggest that the same process degraded nitrite in these experiments. The $\varepsilon$ values obtained in this study are consistent with $\varepsilon$ values reported in the literature for laboratory abiotic nitrite reduction studies, ranging from −19.7 to +16.5 ‰ for nitrite reduction by dissolved Fe(II) plus Fe(II) mineral (Benaiges-Fernandez et al., 2020; Chen et al., 2021; Grabb et al., 2017; Margalef-Marti et al., 2020), −8.6 to +12.9 ‰ for only dissolved Fe(II) (Benaiges-Fernandez et al., 2020; Buchwald et al., 2016; Grabb et al., 2017), and −9.4 to +16.4 ‰ for only Fe(II)-containing minerals (Grabb et al., 2017). In contrast, biotic nitrite reduction processes have yielded isotope fractionation values of −23.5 to −1.0 ‰ ($\varepsilon^{15}$N-$NO_2^-$) and −9.8 to −1.0 ‰ ($\varepsilon^{18}$O-$NO_2^-$) (Brunner et al., 2013; Bryan et al., 1983; Martin and Casciotti, 2016). The Rayleigh distillation equation for $NO_2^-$ and $N_2O$ fractions and the changes in its $\delta^{15}N$ results (Fig. 4D) show that $N_2O$(g) is the final product formed, and fractionation did not affect $N_2O$(aq) diffusion to $N_2O$(g) recovered in the vial headspaces. This is evidenced as the $\delta^{15}N^{bulk}$ composition of the generated $N_2O$ approached the initial $\delta^{15}$N-$NO_2^-$ value (Fig. 4D), which also explains the incomplete 100% $N_2O$ recovery in the headspace vials due to the high solubility of $N_2O$ in water. The natural logarithm of the generated $N_2O$(g) was positive and linearly correlated with the $\delta^{15}N^{bulk}_{N2O(g)}$ with slopes of 3.2 ± 0.2 ‰ in DFe and 4.7 ± 0.6 ‰ in Sid+DFe (Fig. S2). The calculated SP values, 22.5 ± 0.5 ‰ (DFe) and 23.5 ± 0.7 ‰ (Sid+DFe) are consistent with previous findings for chemodenitrification (0 to 30.2 ‰) (Grabb et al., 2017; Li et al., 2022). The SP values determined in this study differ from previously reported SP values associated with heterotrophic denitrification (−5.8 to 8.9‰: Haslun et al., 2018; Li et al., 2022; Rohe et al., 2017; Sutka et al., 2006; Toyoda et al., 2017; Winther et al., 2018; Yamazaki

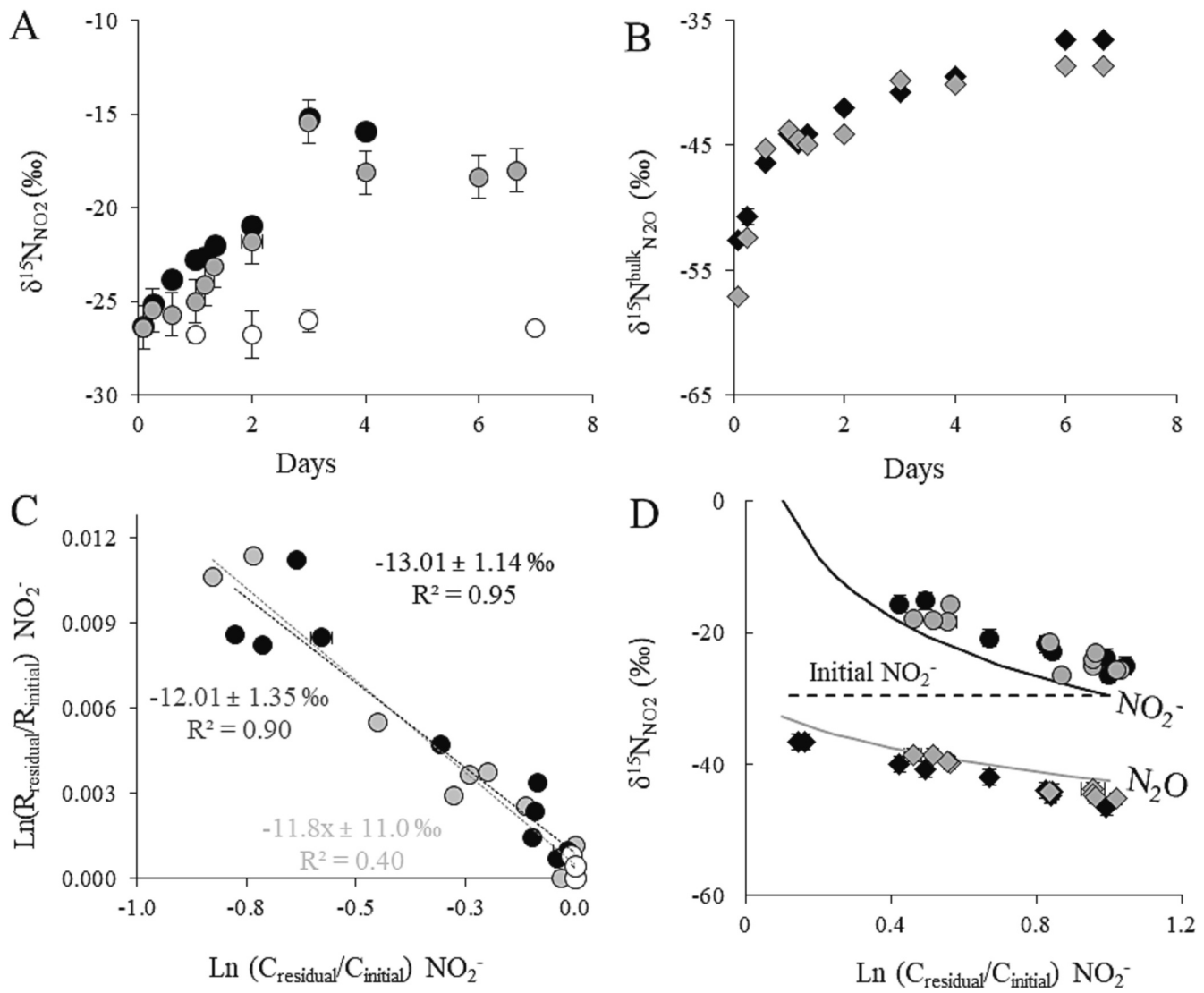


**Fig. 4.** Evolution of $\delta^{15}N_{NO2}$ (A) and $\delta^{15}N^{bulk}_{N2O}$(g) (B) during abiotic nitrite reduction. C) A plot of the natural logarithm of unreacted nitrite fraction against the isotope ratio with slopes indicating the isotope fractionation. D) The Rayleigh distillation model using the average $\varepsilon$ value (12 ‰) and the experimentally analyzed $\delta^{15}N$ of the unreacted $NO_2^-$ and generated $N_2O$. The error bars represent the standard error (SE) of duplicate samples, and non-visible error bars are small and embedded within the data points. Black, grey and white colors indicate Sid+DFe, DFe and Sid experiments, respectively. Circles and diamonds represent experimental results, and solid lines represent the Rayleigh model.

et al., 2014) and nitrifier denitrification (−10 to 0 ‰: Ostrom and Ostrom, 2012), although, they exhibit a similarity to the SP values associated with fungal denitrification (21.9 to 37 ‰: Ostrom and Ostrom, 2012; Rohe et al., 2014), and hydroxylamine oxidation (29 to 33 ‰: Ostrom and Ostrom, 2012; Tischer et al., 2022), but these biological processes are not occurring in our studied systems. Considering the factors mentioned above, we can infer that chemodenitrification is the main process for nitrite reduction in our study, and the isotopic data shows characteristic patterns associated with chemodenitrification process.

Although siderite reactivity with nitrite was almost negligible, it was observed that when it was mixed with dissolved Fe(II), the nitrite removal rate was increased up to 84%, while nitrite removal induced by dissolved Fe(II) alone was 54%. The increased nitrite reduction suggested that siderite might have contributed to the increased chemodenitrification rate, which is consistent with previously conducted studies reporting increased reactivity of Fe(II) in the presence of minerals surfaces (Dhakal et al., 2021; Jones et al., 2014; Rakshit et al., 2016, 2008; Visser et al., 2020). During chemodenitrification, not all the Fe(II) dissolved in water is usually involved in the direct nitrite reduction: some portion may bind to the siderite surface to form reactive surfaces, which acts as a surface catalyst, increasing the Fe(II) electron density improving its potential as a reductant (Jones et al., 2015; Rakshit et al., 2016). Similar to Benaiges-Fernandez et al. (2020) and Chen et al. (2020b), the reduction of nitrite only by dissolved Fe(II) in the DFe batch experiment occurred without a mineral catalyst, which is contrary to earlier reports by Cooper et al. (2003) and Rakshit et al. (2008) that postulated that chemodenitrification required a mineral catalyst. The chemical reduction of nitrite by only Fe(II) involves the electron transfer process. Nitrite, in this process, is bound to Fe(II) to form Fe(II)-$NO_2^-$ complex, where electrons are transferred to nitrite, producing nitrous oxide and Fe(III) oxyhydroxides (Chen et al., 2021; Rakshit et al., 2016).

### 3.2. *Kinetic analyses during abiotic nitrite reduction*

Nitrite concentration evolution with time revealed that nitrite degradation followed a pseudo-first order kinetics with respect to nitrite concentration according to Eq. (4), where $d[NO_2^-]/dt$ is the nitrite degradation rate (mol $L^{-1}$ $s^{-1}$), and $k$ is the pseudo-first-order rate constant ($s^{-1}$). Once integrated, Eq. (4) becomes a linear equation if Ln

$[NO_2^-]$ is expressed as a function of time (Eq. (5)), and then, the rate constant and the initial nitrite concentration can be obtained after a linear regression of the experimental values (Fig. 5A) (Table 2).

$$\frac{d[NO_2^-]}{dt} = -k\cdot[NO_2^-] \quad (4)$$

$$Ln[NO_2^-] = Ln[NO_2^-]_0 - kt \quad (5)$$

The estimated initial nitrite concentrations were 1.21 ± 0.02 mmol $L^{-1}$, 1.11 ± 0.05 mmol $L^{-1}$ and 1.19 ± 0.07 mmol $L^{-1}$ in Sid, DFe and Sid+DFe experiments, respectively (Table 2). These values are very close and consistent with the initial $NO_2^-$ concentration used in the experiments (Table 1). However, *k* values are (4.94 ± 4.85)·$10^{-8}$ $s^{-1}$, (1.48 ± 0.17)·$10^{-6}$ $s^{-1}$, and (3.31 ± 0.20)·$10^{-6}$ $s^{-1}$ for Sid, DFe and Sid+DFe, significantly different between conducted batch experiments (Table 2).

In order to ascertain the dependence of rate constant *k* with Fe(II) aqueous concentration, we have performed preliminary geochemical calculations to estimate Fe(II) aqueous concentration since it was not measured. In the geochemical calculations, the experimental procedure has been reproduced. First, SW (Table 1) was equilibrated with atmospheric $CO_2$(g) ($p_{CO2(g)} = 10^{-3.5}$ atm) and with calcite (in case of oversaturation) as SW was not prepared in a controlled atmosphere. Total aqueous Fe(II) concentration, $[Fe(II)]_T$, was calculated after equilibrating this $CO_2$ equilibrated SW (from now on, CESW) with Fe-minerals before nitrite reduction starts. The amount of initial siderite considered in the calculation was 8.63·$10^{-3}$ mmol $L^{-1}$ in Sid and DFe+Sid experiments, while no siderite was considered to be initially present in the DFe experiment. Moreover, 5 mmol $L^{-1}$ of $FeCl_2{\cdot}4H_2O$ was added to the solution in DFe and Sid+DFe experiments. In all cases, amorphous Fe (III) hydroxide ($Fe(OH)_3$(am)) and calcite were left to precipitate if oversaturated. The composition of the CESW before and after equilibration with Fe-minerals, values of $[Fe(II)]_T$, the remaining amount of siderite and the precipitated $Fe(OH)_3$(am) obtained in these calculations are summarized in Table 3.

The SW pH (7.6) dropped to 6.52, 3.12 and 5.48 in Sid, DFe and Sid+DFe, respectively, after the preliminary calculations. Similarly, the Eh's reduced from 0.17 to −0.13 V in Sid, from 0.69 to 0.08 V in DFe and from 0.25 to −0.08 V Sid+DFe (Fig. S3), showing reducing conditions. These initial conditions are favorable for nitrite reduction as acidic conditions (pH < 6) have often been found to promote nitrite reduction in experimental laboratory studies (Dhakal et al., 2013; Kampschreur et al., 2011).

**Table 2**
Regression analysis for nitrite reduction over time, shown in Fig. 5.

| Experiment | Equation of regression line | $R^2$ |
|---|---|---|
| Sid | $Ln[NO_2^-] = (-4.9 \pm 4.9{\cdot}10^{-8}) \cdot t - (6.7 \pm 0.1)$ | 0.3 |
| DFe | $Ln[NO_2^-] = (-1.48 \pm 0.17{\cdot}10^{-6}) \cdot t - (6.80 \pm 0.05)$ | 0.96 |
| Sid+DFe | $Ln[NO_2^-] = (-3.31 \pm 0.20{\cdot}10^{-6}) \cdot t - (6.70 \pm 0.06)$ | 0.97 |

A plot of the pseudo-first-order constants, k ($s^{-1}$), versus these calculated $[Fe(II)]_T$ (mol $L^{-1}$) shows a positive linear relationship (Fig. 5B), from which the k dependence on Fe concentration can be obtained. Therefore, Eq. (4) can be further developed to Eq. (6), where nitrite degradation rate (mol $L^{-1}$ $s^{-1}$) is a second-order kinetic rate with a constant value of (9.39 ± 0.36)·$10^{-4}$ L $mol^{-1}$ $s^{-1}$.

$$\frac{d[NO_2^-]}{dt} = (9.39 \pm 0.36){\cdot}10^{-4}\cdot[NO_2^-]\cdot[Fe(II)] \quad (6)$$

The k values obtained in the current study (4.94·$10^{-8}$–3.31·$10^{-6}$ $s^{-1}$), according to Eq. (4), were in agreement with the range of values reported in the literature (3.89·$10^{-8}$–2.78·$10^{-5}$ $s^{-1}$; Buchwald et al., 2016; Jones et al., 2014; Rakshit et al., 2008). Additionally, the overall second-order nitrite reduction rate constant (k') calculated for the current batch experiments (9.39·$10^{-4}$ mol $L^{-1}$ $s^{-1}$) according to Eq. (6), was also in concordance with the range of values (1.53·$10^{-4}$–9.38·$10^{-4}$ mol $L^{-1}$ $s^{-1}$) obtained for similar chemodenitrification experiments (Benaiges-Fernandez et al., 2020; Rakshit et al., 2008; Robinson et al., 2021).

### 3.3. Conceptual and numerical model

The model presented in the current study describes the coupled reaction between chemical nitrite reduction and Fe(II) oxidation, linked to the evolution of $NO_2^-$ and $N_2O$ isotopic composition in a fully saturated batch system and at a constant temperature of 25 °C. The linked nitrite reduction and Fe(II) oxidation were considered a single-step process expressed in reaction (R2) and quantified by Eq. (6). This is an overall process simplification, as surface catalytic effects by direct and indirect

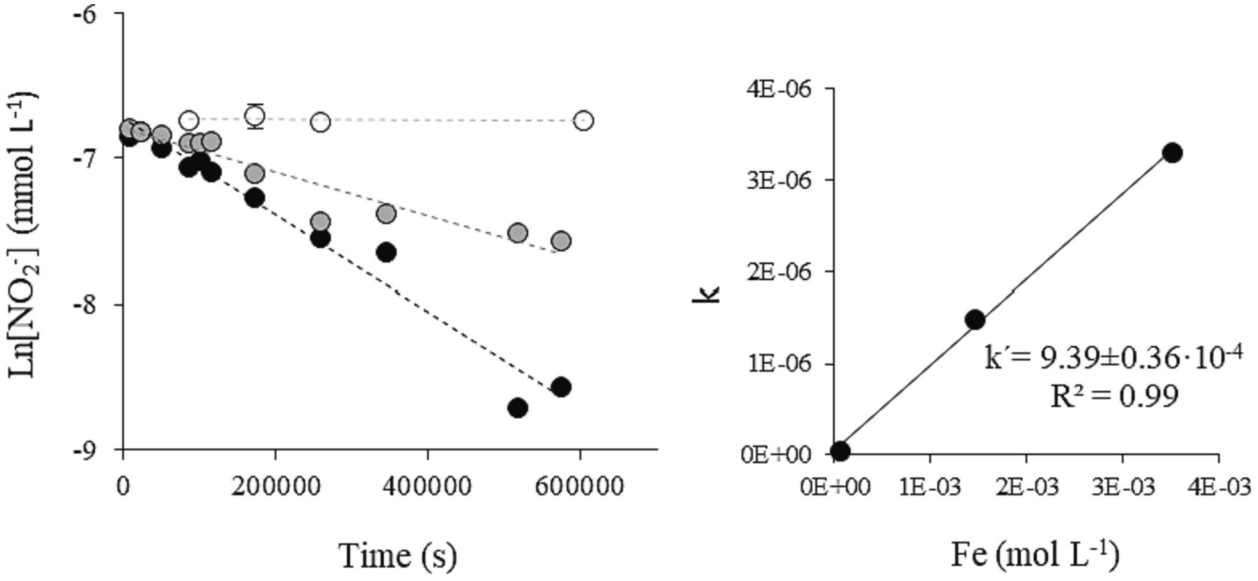


**Fig. 5.** A) Natural logarithm of $NO_2^-$ concentration versus time. B) The pseudo-first-order rate constants versus the total aqueous Fe(II) concentration before $NO_2^-$ reduction. The white, grey and black colors in A represent Sid, DFe and Sid+DFe, respectively. The error bars represent the standard error (SE) of duplicate samples, and non-visible error bars are small and embedded within the data points. The analysis of the regression lines can be seen in Table 2.

**Table 3**
CESW composition before and after equilibrating with Fe-minerals and mineral composition after equilibration for Sid, DFe and Sid+DFe cases.

| Chemicals | pH | Eh V | Ca mM | Mg mM | K mM | Na mM | Cl mM | S mM | P mM | C mM | $Fe(II)_T$ mM | Siderite mM | $Fe(OH)_3$ mM |
|---|---|---|---|---|---|---|---|---|---|---|---|---|---|
| CESW | 8.62 | 0.60 | 0.16 | 1.24 | 2.55 | 6.44 | 5.75 | 1.42 | 0.04 | 2.36 | – | – | – |
| CESW-Sid | 6.53 | 0.17 | 0.16 | 1.24 | 2.55 | 6.44 | 5.75 | 1.42 | 0.04 | 5.95 | 0.05 | 5.04 | 3.54 |
| CESW-DFe | 3.11 | 0.69 | 0.16 | 1.24 | 2.55 | 6.44 | 15.75 | 1.42 | 0.04 | 2.36 | 1.46 | – | 2.42 |
| CESW-Sid+DFe | 5.48 | 0.25 | 0.16 | 1.24 | 2.55 | 6.44 | 15.75 | 1.42 | 0.04 | 4.40 | 3.51 | 6.58 | 3.54 |

sorption onto siderite are not considered in our model. The model does not consider the formation of $N_2O(g)$ neither.

$$2NO_2^- + 6H^+ + 4Fe^{2+} \rightarrow N_2O_{(aq)} + 4Fe^{3+} + 3H_2O \quad (R2)$$

The change in the $\delta^{15}N$ of $NO_2^-$ during nitrite reduction has been modeled according to first-order degradation kinetics described in Van Breukelen and Prommer (2008) (Eq. (7)), where $\varepsilon$ is the experimental kinetic isotope fractionation, $[\delta^{15}N_{NO2}]/([\delta^{15}N_{NO2}] + [\delta^{14}N_{NO2}])$ is N isotopic ratio of $NO_2^-$, and $d[NO_2^-]/dt$ is the $NO_2^-$ degradation rate, calculated from Eq. (6).

$$R_{\delta\ HEA} = \frac{d[NO_2^-]}{dt} \cdot \frac{[\delta\ 15N_{NO2}]}{[\delta\ 15N_{NO2}] + [\delta\ 14N_{NO2}]} \cdot \varepsilon \quad (7)$$

The prepared water composition obtained after the initial geochemical calculations) (Table 3) with an initial nitrite concentration of 1.18 mol $L^{-1}$ and the amounts of siderite and amorphous Fe(III) hydroxide indicated in Table 3 have been considered as initial conditions for the different batch experiments. In all cases, siderite, calcite and amorphous Fe(III) hydroxide are left to precipitate or dissolve in equilibrium. The average isotopic fractionation value from the experimental data ($\varepsilon$ of −12.0 ‰) was considered for Eq. (7). According to the experimental data, all the models were run for 7 days in 70 equal steps. Sensitivity cases have been run to account for k uncertainties.

The models well reproduced nitrite concentration experimental results in Sid, DFe and Sid+DFe. The same initial nitrite concentration, which was taken as the average of three experimental sets, was slightly lower compared to the initial nitrite concentration of the Sid experiments, which accounts for the high nitrite experimental results. Similar to the experimental data, 5–6%, 61–63%, and 84–86% of nitrite is removed in Sid, DFe and Sid+DFe, respectively, and was paralleled with an increase of $\delta^{15}N_{NO2}$ value from −26.9 to −26.1 ± 0.3 ‰ (Sid), −15.3 ± 0.5 ‰ (DFe) and − 4.2 ± 0.8 ‰ (Sid+DFe) in the remaining nitrite (Fig. 6A). The isotope model could simulate $\delta^{15}N_{NO2}$ at low $NO_2^-$ concentrations, below analytical capabilities.

As the models simulate the total aqueous $N_2O$ generated in the solution, modeled results overestimate measured $N_2O(g)$, as experimental results measure the $N_2O$ diffused from the solution into the HS, which only occurs in a small percentage (Fig. 6B). However, considering the total $N_2O$ calculated using Henry's Law, comprising both the gas and liquid phases $N_2O$, the results align closely with the model results for DFe and Sid, but slightly lower in the Sid+DFe (Fig. 6B).

Geochemical calculation with the GibbsStudio software indicated that amorphous Fe-oxyhydroxide was formed in all the batch experiments. $Fe(OH)_3(am)$ slightly increased from 3.5 to 3.7 mmol $L^{-1}$ in Sid and significantly increased from 2.2 to 2.9 mmol $L^{-1}$ in DFe and 3.5 to 5.5 mmol $L^{-1}$ in Sid+DFe. 0.1 and 1.5 mmol $L^{-1}$ of siderite were dissolved in Sid and Sid+DI, respectively, and calcite did not form in any of the models due to the low concentration of Ca ions in SW (Table 2). In DFe and Sid+DFe models, more Fe(II) was oxidized, resulting in a higher rate of nitrite reduction, forming more Fe-oxyhydroxides, which is consistent with the experimental data as brown precipitates were observed in DFe and Sid+DFe experiments. The small amount of siderite dissolved in Sid explains the slow nitrite reduction, as siderite dissolution is the only Fe(II) source. On the other hand, the large amount of dissolved siderite in Sid+DFe may also contribute to improving nitrite reduction, which is often observed in iron-rich environments (Buchwald et al., 2016; Jones et al., 2015).

The numerical model could predict concentrations below detection by our analytical techniques. While nitrous oxide was not detected in the headspace of vials in the Sid experiments, the model successfully

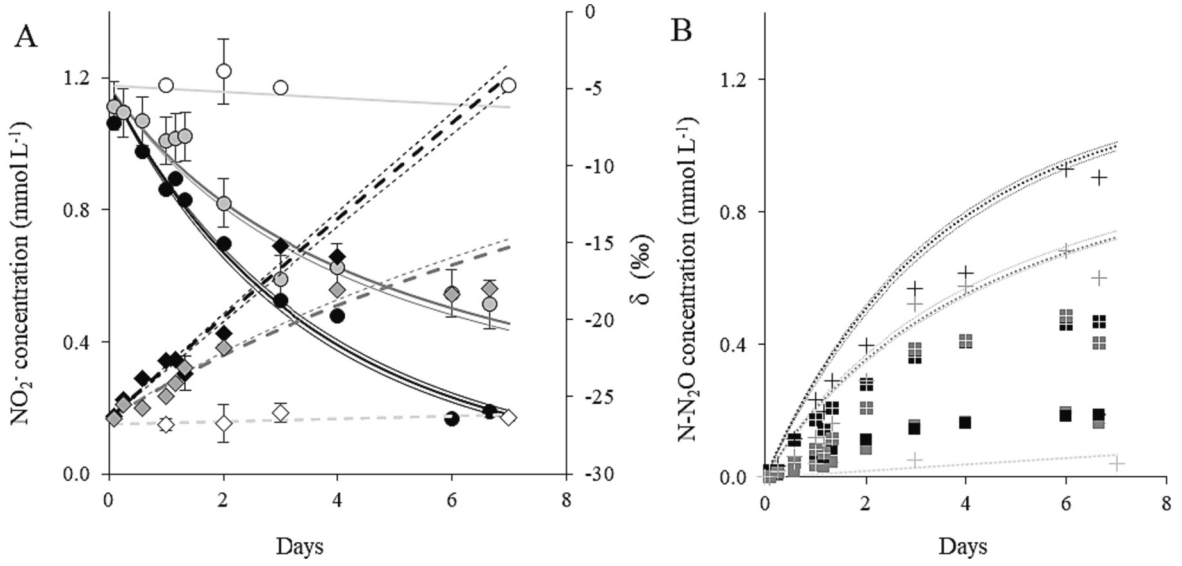


**Fig. 6.** A) $NO_2^-$ concentration and $\delta^{15}N_{NO2}$ evolution over time for the three experiments. White, grey and black colors represent Sid, DFe and Sid+DFe, whereas circles and diamonds indicate experimental $NO_2^-$ and $\delta^{15}N_{NO2}$, respectively, and lines are model results. B) Recovered N-$N_2O$ in gas phase (squares), calculated N-$N_2O$ in liquid phase (plus inside squares), transformed N (plus) and simulated total N-$N_2O$ (lines) evolution over time. The thin outer lines represent the uncertainty due to constant rate error. The error bars represent the standard error (SE) of duplicate samples, and non-visible error bars are small and embedded within the data points.

predicted small amount of aqueous nitrous oxide concentration. Consequently, it would be intriguing to consider monitoring the aqueous nitrous oxide concentration in future denitrification and chemo-denitrification experiments. At the laboratory scale, it will require a long time to study nitrite reactivity with only siderite due to the low reactivity as in our case, but our numerical model provides an essential advantage of its ability to predict the reactivity of nitrite and only siderite over extended periods beyond the laboratory range. Our model could also be used as a tool for similar experimental studies and field applications.

## 4. Conclusions

This study investigated the reaction of $NO_2^-$ by Fe(II) oxidation using chemical, isotopic data and numerical modeling. Results showed that the reactivity of siderite alone was low, removing only 3% of nitrite from the water. Dissolved Fe(II) induced nitrite reduction without a mineral catalyst, achieving 54% of nitrite removal. The $NO_2^-$ reduction rate was enhanced when dissolved Fe(II) was mixed with siderite, removing 84% of nitrite from the solution. The calculated nitrogen of nitrous oxide in the gas and liquid phases was equal to the nitrite nitrogen transformed in water, showing that $N_2O$ was the final product generated. This also suggested $N_2O$ leakage through the butyl rubber stoppers, and the formation of intermediary NO did not occur in our experiments. Henry's Law showed that 50 to 98% of the total $N_2O$ generated in water was dissolved, and low $N_2O$ recovery in the headspace of the vials was attributed mainly to low diffusion of aqueous $N_2O$. The isotopic fractionation ($\varepsilon$) and site preference (SP) values calculated were $-12.0 \pm 1.4$ ‰ and $22.5 \pm 0.7$ ‰ for DFe, respectively, whereas for Sid+DFe were $-13.0 \pm 1.1$ ‰ ($\varepsilon$) and $23.5 \pm 0.5$ ‰ (SP). The isotopic data in this study showed that the main process for nitrite reduction in the experiments was chemodenitrification.

The present study developed a geochemical model describing the oxidation-reduction reaction between Fe(II) and nitrite and nitrous oxide production according to a second-order kinetics that could simulate the experimental results. The evolution of $\delta^{15}N$ of $NO_2^-$ was reproduced following the first-order kinetics. The experimental conditions of our study, coupled with nitrite and nitrous oxide isotopic data, the Rayleigh distillation equation and the geochemical model complementary tools, showed that chemodenitrification was the main nitrite attenuation process and that the influence of biological processes was limited. This study underscores the applicability of abiotic nitrite reduction concentration and isotope models across diverse experimental and field scenarios to understand nitrogen species reaction abiotic pathways.

## CRediT authorship contribution statement

**Alex Abu:** Data curation, Formal analysis, Writing – original draft. **Raúl Carrey:** Conceptualization, Data curation, Formal analysis, Supervision, Writing – review & editing. **Dídac Navarro-Ciurana:** Supervision, Writing – review & editing. **Rosanna Margalef-Marti:** Conceptualization, Data curation, Formal analysis, Writing – review & editing. **Albert Soler:** Funding acquisition, Writing – review & editing. **Neus Otero:** Funding acquisition, Writing – review & editing. **Cristina Domènech:** Conceptualization, Data curation, Formal analysis, Funding acquisition, Supervision, Writing – review & editing.

## Declaration of competing interest

The authors declare that they have no known competing financial interests or personal relationships that could have appeared to influence the work reported in this paper.

## Data availability

Data will be made available on request.

## Acknowledgements

This work is part of the research project ISOREM (REMEDIATE) (TED2021-131005B-C31) funded by MCIN/AEI/10.13039/501100011033 and by "European Union NextGenerationEU/PRTR" and the grant PACE-ISOTEC (CGL2017-87216-C4-1-R) funded by MCIN/AEI/10.13039/501100011033 and by "ERDF A way of making Europe". Support for the research was also received through the project 2021-SGR-00308 (Consolidate Research Group MAGH) from the Catalan Government. The authors are grateful for the analytical support of the Centres Científics i Tecnològics de la Universitat de Barcelona (CCiT-UB). Abu Alex would also like to thank the Agència de Gestió d'Ajuts Universitaris i de Recerca de la Generalitat de Catalunya (2019 FI_B 01059) for the PhD grant and L'Institut de Recerca de l'Aigua (IdRA)-Universitat de Barcelona for their support.

## Appendix A. Supplementary data

Supplementary data to this article can be found online at https://doi.org/10.1016/j.chemgeo.2024.121942.

## References

Arauzo, M., 2017. Vulnerability of groundwater resources to nitrate pollution: a simple and effective procedure for delimiting Nitrate Vulnerable zones. Sci. Total Environ. 575, 799–812. https://doi.org/10.1016/j.scitotenv.2016.09.139.

Benaiges-Fernandez, R., Offeddu, F.G., Margalef-Marti, R., Palau, J., Urmeneta, J., Carrey, R., Otero, N., Cama, J., 2020. Geochemical and isotopic study of abiotic nitrite reduction coupled to biologically produced Fe(II) oxidation in marine environments. Chemosphere 260, 127554. https://doi.org/10.1016/j.chemosphere.2020.127554.

Betlach, M.R., Tiedje, J.M., 1981. Kinetic Explanation for Accumulation of Nitrite, Nitric Oxide, and Nitrous Oxide during Bacterial Denitrification. Appl. Environ. Microbiol. 42, 1074–1084. https://doi.org/10.1128/aem.42.6.1074-1084.1981.

Brunner, B., Contreras, S., Lehmann, M.F., Matantseva, O., Rollog, M., Kalvelage, T., Klockgether, G., Lavik, G., Jetten, M.S.M., Kartal, B., Kuypers, M.M.M., 2013. Nitrogen isotope effects induced by anammox bacteria. Proc. Natl. Acad. Sci. U. S. A. 110, 18994–18999. https://doi.org/10.1073/pnas.1310488110.

Bryan, B.A., Shearer, G., Skeeters, J.L., Kohl, D.H., 1983. Variable expression of the nitrogen isotope effect associated with denitrification of nitrite. J. Biol. Chem. 258, 8613–8617. https://doi.org/10.1016/s0021-9258(18)32100-8.

Bryce, C., Blackwell, N., Schmidt, C., Otte, J., Huang, Y.M., Kleindienst, S., Tomaszewski, E., Schad, M., Warter, V., Peng, C., Byrne, J.M., Kappler, A., 2018. Microbial anaerobic Fe(II) oxidation – Ecology, mechanisms and environmental implications. Environ. Microbiol. 20, 3462–3483. https://doi.org/10.1111/1462-2920.14328.

Buchwald, C., Casciotti, K.L., 2010. Oxygen isotopic fractionation and exchange during bacterial nitrite oxidation. Limnol. Oceanogr. 55, 1064–1074. https://doi.org/10.4319/lo.2010.55.3.1064.

Buchwald, C., Grabb, K., Hansel, C.M., Wankel, S.D., 2016. Constraining the role of iron in environmental nitrogen transformations: dual stable isotope systematics of abiotic NO2- reduction by Fe(II) and its production of N2O. Geochim. Cosmochim. Acta 186, 1–12. https://doi.org/10.1016/j.gca.2016.04.041.

Casciotti, K.L., McIlvin, M., Buchwald, C., 2010. Oxygen isotopic exchange and fractionation during bacterial ammonia oxidation. Limnol. Oceanogr. 55, 1805. https://doi.org/10.4319/lo.2010.55.4.1805.

Chen, G., Chen, D., Li, F., Liu, T., Zhao, Z., Cao, F., 2020a. Dual nitrogen-oxygen isotopic analysis and kinetic model for enzymatic nitrate reduction coupled with Fe(II) oxidation by Pseudogulbenkiania sp. strain 2002. Chem. Geol. 534, 119456 https://doi.org/10.1016/j.chemgeo.2019.119456.

Chen, D., Yuan, X., Zhao, W., Luo, X., Li, F., Liu, T., 2020b. Chemodenitrification by Fe (II) and nitrite: pH effect, mineralization and kinetic modeling. Chem. Geol. 541 https://doi.org/10.1016/j.chemgeo.2020.119586.

Chen, G., Zhao, W., Yang, Y., Chen, D., Wang, Y., Li, F., Zhao, Z., Cao, F., Liu, T., 2021. Chemodenitrification by Fe(II) and nitrite: Effects of temperature and dual N[and]O isotope fractionation. Chem. Geol. 575, 120258 https://doi.org/10.1016/j.chemgeo.2021.120258.

Collman, J.P., Dey, A., Yang, Y., Decréau, R.A., Ohta, T., Solomon, E.I., 2008. Intermediates involved in the two electron reduction of NO to N 2O by a functional synthetic model of heme containing bacterial NO reductase. J. Am. Chem. Soc. 130, 16498–16499. https://doi.org/10.1021/ja807700n.

Cooper, D.C., Picardal, F.W., Schimmelmann, A., Coby, A.J., 2003. Chemical and Biological Interactions during Nitrate and Goethite Reduction by Shewanella

putrefaciens 200. Appl. Environ. Microbiol. 69, 3517–3525. https://doi.org/10.1128/AEM.69.6.3517.
Dhakal, P., Matocha, C.J., Huggins, F.E., Vandiviere, M.M., 2013. Nitrite reactivity with magnetite. Environ. Sci. Technol. 47, 6206–6213. https://doi.org/10.1021/es304011w.
Dhakal, P., Coyne, M.S., McNear, D.H., Wendroth, O.O., Vandiviere, M.M., D'Angelo, E. M., Matocha, C.J., 2021. Reactions of nitrite with goethite and surface Fe(II)-goethite complexes. Sci. Total Environ. 782, 146406 https://doi.org/10.1016/j.scitotenv.2021.146406.
Dunlop, D.J., Özdemir, Ö., 2015. Magnetizations in rocks and minerals. In: Treatise on Geophysics: Second Edition, pp. 255–308. https://doi.org/10.1016/B978-0-444-53802-4.00102-0.
Emerson, D., Fleming, E.J., McBeth, J.M., 2010. Iron-oxidizing bacteria: an environmental and genomic perspective. Annu. Rev. Microbiol. 64, 561–583. https://doi.org/10.1146/annurev.micro.112408.134208.
EU parliament, 2020. Directive (EU) 2020/2184 of the European Parliament and of the Council of 16 December 2020 on the quality of water intended for human consumption. Off. J. Eur. Union 2019, 1–62.
Fan, A.M., Steinberg, V.E., 1996. Health implications of nitrate and nitrite in drinking water: an update on methemoglobinemia occurrence and reproductive and developmental toxicity. Regul. Toxicol. Pharmacol. 23, 35–43. https://doi.org/10.1006/rtph.1996.0006.
Grabb, K.C., Buchwald, C., Hansel, C.M., Wankel, S.D., 2017. A dual nitrite isotopic investigation of chemodenitrification by mineral-associated Fe(II) and its production of nitrous oxide. Geochim. Cosmochim. Acta 196, 388–402. https://doi.org/10.1016/j.gca.2016.10.026.
Granger, J., Wankel, S.D., 2016. Isotopic overprinting of nitrification on denitrification as a ubiquitous and unifying feature of environmental nitrogen cycling. Proc. Natl. Acad. Sci. U. S. A. 113, E6391–E6400. https://doi.org/10.1073/pnas.1601383113.
Grau-Martínez, A., Torrentó, C., Carrey, R., Soler, A., Otero, N., 2019. Isotopic evidence of nitrate degradation by a zero-valent iron permeable reactive barrier : batch experiments and a field scale study. J. Hydrol. 570, 69–79. https://doi.org/10.1016/j.jhydrol.2018.12.049.
Haslun, J.A., Ostrom, N.E., Hegg, E.L., Ostrom, P.H., 2018. Estimation of isotope variation of N2O during denitrification by Pseudomonas aureofaciens and Pseudomonas chlororaphis: Implications for N2O source apportionment. Biogeosciences 15, 3873–3882. https://doi.org/10.5194/bg-15-3873-2018.
Heil, J., Wolf, B., Bru, N., Emmenegger, L., Vereecken, H., Mohn, J., 2014. Site-specific N isotopic signatures of abiotically produced N2O, 139, pp. 72–82. https://doi.org/10.1016/j.gca.2014.04.037.
Jones, A.M., Griffin, P.J., Collins, R.N., Waite, T.D., 2014. Ferrous iron oxidation under acidic conditions - the effect of ferric oxide surfaces. Geochim. Cosmochim. Acta 145, 1–12. https://doi.org/10.1016/j.gca.2014.09.020.
Jones, L.C., Peters, B., Lezama Pacheco, J.S., Casciotti, K.L., Fendorf, S., 2015. Stable isotopes and iron oxide mineral products as markers of chemodenitrification. Environ. Sci. Technol. 49, 3444–3452. https://doi.org/10.1021/es504862x.
Kampschreur, M.J., Kleerebezem, R., de Vet, W.W.J.M., Van Loosdrecht, M.C.M., 2011. Reduced iron induced nitric oxide and nitrous oxide emission. Water Res. 45, 5945–5952. https://doi.org/10.1016/j.watres.2011.08.056.
Kappler, A., Straub, K.L., 2005. Geomicrobiological cycling of iron. Mol. Geomicrobiol. 59, 85–108. https://doi.org/10.2138/rmg.2005.59.5.
Kendall, C., Elliott, E.M., Wankel, S.D., 2007. Tracing anthropogenic inputs of nitrogen to ecosystems. In: Stable Isotopes in Ecology and Environmental Science, pp. 375–449. https://doi.org/10.1002/9780470691854.ch12.
Kopf, S.H., Henny, C., Newman, D.K., 2013. Ligand-enhanced abiotic iron oxidation and the effects of chemical versus biological iron cycling in anoxic environments. Environ. Sci. Technol. 47, 2602–2611. https://doi.org/10.1021/es3049459.
Li, S., Wang, S., Ji, G., 2022. Influences of carbon sources on N2O production during denitrification in freshwaters: activity, isotopes and functional microbes. Water Res. 226, 119315 https://doi.org/10.1016/j.watres.2022.119315.
Liu, T., Chen, D., Luo, X., Li, X., Li, F., 2019. Microbially mediated nitrate-reducing Fe(II) oxidation: Quantification of chemodenitrification and biological reactions. Geochim. Cosmochim. Acta 256, 97–115. https://doi.org/10.1016/j.gca.2018.06.040.
Margalef-Marti, R., Carrey, R., Benito, J.A., Marti, V., Soler, A., Otero, N., 2020. Nitrate and nitrite reduction by ferrous iron minerals in polluted groundwater: Isotopic characterization of batch experiments. Chem. Geol. 548, 119691 https://doi.org/10.1016/j.chemgeo.2020.119691.
Margalef-Marti, R., Llovet, A., Carrey, R., Ribas, A., Domene, X., Mattana, S., Chin-Pampillo, J., Mondini, C., Alcañiz, J.M., Soler, A., Otero, N., 2021. Impact of fertilization with pig slurry on the isotopic composition of nitrate retained in soil and leached to groundwater in agricultural areas. Appl. Geochem. 125 https://doi.org/10.1016/j.apgeochem.2020.104832.
Mariotti, A., Germon, J.C., Hubert, P., Kaiser, P., Letolle, R., Tardieux, A., Tardieux, P., 1981. Experimental determination of nitrogen kinetic isotope fractionation: some principles; illustration for the denitrification and nitrification processes. Plant Soil 62, 413–430. https://doi.org/10.1007/BF02374138.
Martin, T.S., Casciotti, K.L., 2016. Nitrogen and oxygen isotopic fractionation during microbial nitrite reduction. Limnol. Oceanogr. 61, 1134–1143. https://doi.org/10.1002/lno.10278.
McIlvin, M.R., Altabet, M.A., 2005. Chemical conversion of nitrate and nitrite to nitrous oxide for nitrogen and oxygen isotopic analysis in freshwater and seawater. Anal. Chem. 77, 5589–5595. https://doi.org/10.1021/ac050528s.
Nardi, A., de Vries, L.M., 2017. GibbsStudio. Barcelona Science Technologies SL, Barcelona, Spain.
Nowak, J., Szubka, M., Klimontko, J., Mariola, K., 2023. Thermal decomposition of siderite and characterization of the decomposition products under O2 and CO2 atmospheres. Minerals 13, 1066. https://doi.org/10.3390/min13081066.
Ostrom, N.E., Ostrom, P.H., 2012. The isotopomers of nitrous oxide: analytical considerations and application to resolution of microbial production pathways. Adv. Isotope Geochem. 453–476. https://doi.org/10.1007/978-3-642-10637-8_23.
Parkhurst, D.L., Appelo, C.A.J., 2013. Description of Input and Examples for PHREEQC Version 3: A Computer Program for Speciation, Batch-Reaction, One-Dimensional Transport, and Inverse Geochemical Calculations. U.S. Geological Survey. https://doi.org/10.1097/00000446-195210000-00005.
Picardal, F., 2012. Abiotic and microbial interactions during anaerobic transformations of Fe(II) and NOx. Front. Microbiol. 3, 1–7. https://doi.org/10.3389/fmicb.2012.00112.
Rahman, M.M., Roberts, K.L., Grace, M.R., Kessler, A.J., Cook, P.L.M., 2019. Role of organic carbon, nitrate and ferrous iron on the partitioning between denitrification and DNRA in constructed stormwater urban wetlands. Sci. Total Environ. 666, 608–617. https://doi.org/10.1016/j.scitotenv.2019.02.225.
Rakshit, S., Matocha, C.J., Coyne, M.S., 2008. Nitrite reduction by siderite. Soil Sci. Soc. Am. J. 72, 1070–1077. https://doi.org/10.2136/sssaj2007.0296.
Rakshit, S., Matocha, C.J., Coyne, M.S., Sarkar, D., 2016. Nitrite reduction by Fe(II) associated with kaolinite. Int. J. Environ. Sci. Technol. 13, 1329–1334. https://doi.org/10.1007/s13762-016-0971-x.
Robinson, T., Latta, D.E., Notini, L., Schilling, K.E., Scherer, M.M., 2021. Abiotic reduction of nitrite by Fe(II): a comparison of rates and N2O production Thomas. Environ. Sci. https://doi.org/10.1039/d1em00222h.
Rohe, L., Anderson, T.H., Braker, G., Flessa, H., Giesemann, A., Lewicka-Szczebak, D., Wrage-Mönnig, N., Well, R., 2014. Dual isotope and isotopomer signatures of nitrous oxide from fungal denitrification - a pure culture study. Rapid Commun. Mass Spectrom. 28, 1893–1903. https://doi.org/10.1002/rcm.6975.
Rohe, L., Well, R., Lewicka-Szczebak, D., 2017. Use of oxygen isotopes to differentiate between nitrous oxide produced by fungi or bacteria during denitrification. Rapid Commun. Mass Spectrom. 31, 1297–1312. https://doi.org/10.1002/rcm.7909.
Ryabenko, E., Altabet, M.A., Wallace, D.W.R., 2009. Effect of chloride on the chemical conversion of nitrate to nitrous oxide for $\delta^{15}N$ analysis. Limnol. Oceanogr. Methods 7, 545–552. https://doi.org/10.4319/lom.2009.7.545.
Sebilo, M., Billen, G., Mayer, B., Billiou, D., Grably, M., Garnier, J., Mariotti, A., 2006. Assessing nitrification and denitrification in the seine river and estuary using chemical and isotopic techniques. Ecosystems 9, 564–577. https://doi.org/10.1007/s10021-006-0151-9.
Sebilo, M., Aloisi, G., Mayer, B., Perrin, E., Vaury, V., Mothet, A., Laverman, A.M., 2019. Controls on the isotopic composition of nitrite ($\delta^{15}N$ and $\delta^{18}O$) during denitrification in freshwater sediments. Sci. Rep. 9, 1–14. https://doi.org/10.1038/s41598-019-54014-3.
Sørensen, J., Thorling, L., 1991. Stimulation by lepidocrocite (7-FeOOH) of Fe(II)-dependent nitrite reduction. Geochim. Cosmochim. Acta 55, 1289–1294. https://doi.org/10.1016/0016-7037(91)90307-Q.
Sutka, R.L., Ostrom, N.E., Ostrom, P.H., Breznak, J.A., Gandhi, H., Pitt, A.J., Li, F., 2006. Distinguishing nitrous oxide production from nitrification and denitrification on the basis of isotopomer abundances. Appl. Environ. Microbiol. 72, 638–644. https://doi.org/10.1128/AEM.72.1.638-644.2006.
Tischer, J., Zopfi, J., Frey, C., Magyar, P.M., Brand, A., Oswald, K., Jegge, C., Frame, C. H., Miracle, M.R., Sòria-Perpinyà, X., Vicente, E., Lehmann, M.F., 2022. Isotopic signatures of biotic and abiotic N2O production and consumption in the water column of meromictic, ferruginous Lake La Cruz (Spain). Limnol. Oceanogr. 67, 1760–1775. https://doi.org/10.1002/lno.12165.
Toyoda, S., Yoshida, N., Koba, K., 2017. Isotopocule analysis of biologically produced nitrous oxide in various environments. Mass Spectrom. Rev. 36 (2), 32, 135–160. https://doi.org/10.1002/mas.
Van Breukelen, B.M., Prommer, H., 2008. Beyond the Rayleigh equation: reactive transport modeling of isotope fractionation effects to improve quantification of biodegradation. Environ. Sci. Technol. 42, 2457–2463. https://doi.org/10.1021/es071981j.
Visser, A.N., Wankel, S.D., Niklaus, P.A., Byrne, J.M., Kappler, A.A., Lehmann, M.F., 2020. Impact of reactive surfaces on the abiotic reaction between nitrite and ferrous iron and associated nitrogen and oxygen isotope dynamics. Biogeosciences 17, 4355–4374. https://doi.org/10.5194/bg-17-4355-2020.
Wankel, S.D., Ziebis, W., Buchwald, C., Charoenpong, C., Beer, De, Dentinger, J., Xu, Z., Zengler, K., 2017. Evidence for fungal and chemodenitrification based N2O flux from nitrogen impacted coastal sediments. Nat. Commun. 8, 1–11. https://doi.org/10.1038/ncomms15595.
WHO, 2017. Guidelines for Drinking-Water Quality: Fourth Edition Incorporating the First Addendum. Guidel. Drink. Qual. Fourth Ed. Inc. First Add, p. 541.
Winther, M., Balslev-Harder, D., Christensen, S., Priemé, A., Elberling, B., Crosson, E., Blunier, T., 2018. Continuous measurements of nitrous oxide isotopomers during incubation experiments. Biogeosciences 15, 767–780. https://doi.org/10.5194/bg-15-767-2018.
Wrage, N., Velthof, G.L., Van Beusichem, M.L., Oenema, O., 2001. Role of nitrifier denitrification in the production of nitrous oxide. Soil Biol. Biochem. 33, 1723–1732. https://doi.org/10.1016/S0038-0717(01)00096-7.
Yamazaki, T., Hozuki, T., Arai, K., Toyoda, S., Koba, K., Fujiwara, T., Yoshida, N., 2014. Isotopomeric characterization of nitrous oxide produced by reaction of enzymes extracted from nitrifying and denitrifying bacteria. Biogeosciences 11, 2679–2689. https://doi.org/10.5194/bg-11-2679-2014.
Zhu, C., 2012. Geochemical modeling in environmental and geological studies. In: Encyclopedia of Sustainability Science and Technology, pp. 4094–4104. https://doi.org/10.1007/978-1-4419-0851-3.